

Comparing Small Water Bodies' Impact on Subtropical Campus Outdoor Temperature: Measured vs. Simulated Data

Ming-Cheng Liao, Wen-Pei Sung * and Qing-Qing Chen Shi

Department of Landscape Architecture, National Chin Yi University of Technology, No. 57, Sec. 2, Chung Shan Rd., Taiping, Taichung 411030, Taiwan; liaomc@ncut.edu.tw (M.-C.L.); csqq12345@gmail.com (Q.-Q.C.S.)

* Correspondence: wps@ncut.edu.tw

Abstract: This study investigates the impact of small water bodies on outdoor temperatures in their vicinity, using a campus located in the subtropical region of Taichung City, Taiwan, as the research subject. By employing on-site measurements and Computational Fluid Dynamics (CFD) simulations, we examined their temporal and spatial influence, as well as comparisons between actual measurements and software predictions. Key findings include the following: (1) Small water bodies exhibit discernible temperature-regulating effects on their surrounding areas. While the influence diminishes with distance, this attenuation is not stark, and is potentially constrained by the water body's patch size. (2) Regulatory effects vary between day and night. In summer, temperature reductions of up to 3.5 °C (simulated) and 3.2 °C (measured) were observed. Conversely, in winter, daytime temperatures around water bodies may rise by up to 3.9 °C. (3) Discrepancies between CFD simulations and actual measurements, influenced by fluctuations in Global Horizontal Irradiation (GHI), range from +2.5 °C to −1.8 °C. During high GHI periods, measured values surpass simulations, whereas during low or zero GHI conditions, simulations exceed measurements. Moreover, high regression analysis R² values validate the feasibility of CFD simulations for predicting water body-induced temperature changes. Insights from this study offer valuable guidance for urban planners and policymakers seeking sustainable urban climate management strategies.

Keywords: urban heat island effect; water body patch; computational fluid dynamics (CFD); outdoor thermal comfort; global horizontal irradiation (GHI)



Citation: Liao, M.-C.; Sung, W.-P.; Chen Shi, Q.-Q. Comparing Small Water Bodies' Impact on Subtropical Campus Outdoor Temperature: Measured vs. Simulated Data. *Buildings* **2024**, *14*, 1288. <https://doi.org/10.3390/buildings14051288>

Academic Editor: Derek Clements-Croome

Received: 6 April 2024
Revised: 28 April 2024
Accepted: 30 April 2024
Published: 2 May 2024



Copyright: © 2024 by the authors. Licensee MDPI, Basel, Switzerland. This article is an open access article distributed under the terms and conditions of the Creative Commons Attribution (CC BY) license (<https://creativecommons.org/licenses/by/4.0/>).

1. Introduction

The world's population is growing rapidly and increasingly concentrated in cities. Approximately half of the world's population now resides in urban areas. By 2030, it is projected that over 60% of the global population will live in cities [1], with this proportion potentially reaching 68.4% by 2050. Urbanization has resulted in the transformation of natural land cover into artificial surfaces, predominantly comprised of buildings and roads. Moreover, significant anthropogenic heat release disrupts the balance of surface heat energy [2,3], altering the urban microclimate. In contrast to surrounding rural and undeveloped regions, urban areas typically exhibit higher temperatures, particularly during night-time [4]. This phenomenon is commonly referred to as the urban heat island (UHI) effect. The intensity of the UHI effect escalates with the expansion of urban areas, and exacerbates the severity of global warming. The Intergovernmental Panel on Climate Change (IPCC) projects that global average surface temperatures could rise by 4.8 °C by 2100 [5]. However, due to the elevated outdoor temperatures resulting from the UHI effect, there is a growing demand for air conditioning to maintain indoor thermal comfort, leading to a sharp increase in energy consumption in urban areas [6–8]. Prior research suggests that the UHI effect may exacerbate the impact of heatwaves, affecting the health of urban residents [9–11], and contributing to issues such as physical discomfort and respiratory difficulties [12–14].

The strength of the urban heat island (UHI) effect primarily depends on the nature of the land surface and its utilization [15]. Generally, the UHI effect can be mitigated, and outdoor temperatures can be reduced by increasing green space, planting vegetation, using permeable pavement, incorporating water bodies, and employing other means [16]. Recently, urban green infrastructure has garnered attention as a nature-based solution. Urban green infrastructure can effectively absorb a significant amount of heat through the moisture it contains, thereby lowering outdoor temperatures through evapotranspiration [17,18]. For instance, cool roofs can decrease the environmental temperature of urban street canyons, particularly in densely populated cities [19,20]. In comparison to green infrastructure, the mitigation effect of water bodies on the urban heat island (UHI) effect has received less study [21]. However, water bodies primarily impact the urban thermal environment by cooling the air through evaporation [22], which can provide a more potent cooling effect than the green infrastructure described earlier [23,24]. Moreover, the cooling effect of water bodies may vary in different seasons, but it tends to be more consistent [25]. Water bodies are better able to maintain the surrounding air temperature at an appropriate level [26], mitigate high temperatures in cities, and enhance outdoor thermal comfort [27–29].

Variations in the cooling effect of water bodies can be observed in temperature differences between day and night as well as at different distances [30,31]. This variation is primarily influenced by fluctuations in Global Horizontal Irradiation (GHI), leading to inconsistencies in the cooling effect between day and night [32,33]. Related studies suggest that air temperatures near water bodies may even rise at night [34]. In terms of spatial effects, the cooling impact of water bodies tends to decrease with increasing distance, often up to a horizontal distance of 1 km. The shape and size of the water body can significantly influence this effect [35]. Previous studies have identified three main aspects of water bodies related to their influence range, temperature reduction, and temperature gradient. For example, in Shanghai, China, the average influence range of eighteen lakes and three rivers is 0.74 km, with a temperature drop of 3.32 °C and a temperature gradient of 5.15 °C/km. Furthermore, lakes exhibit a significantly stronger cooling effect compared to rivers. Additionally, factors such as the geometric shape of the water body, the presence of ground vegetation in the surrounding area, and the extent of impermeable surfaces are important determinants of the cold island effect associated with water bodies [36].

Water bodies can effectively regulate the urban climate, mitigate the urban heat island effect, and dissipate heat from the surrounding environment through evapotranspiration. The higher heat capacity of water bodies also helps stabilize the surrounding air temperature, preventing excessive daytime heating due to solar radiation. Larger water body patches typically provide a stronger cooling effect. However, due to land scarcity, significantly increasing the area of water bodies within dense urban areas to mitigate the urban heat island effect presents challenges [37]. From another perspective, in less developed urban areas, such as urban campuses, can the same cooling effect be achieved by dividing large water body patches into smaller ones? This study takes Taiwan, located in a subtropical region, as an example. With over three-quarters of its land area consisting of high mountains and hills, the developed flat urban areas in Taiwan are densely populated. Additionally, Taiwan's subtropical climate has contributed to increasingly severe urban heat island effects in recent years. Properly incorporating water bodies into urban areas may help alleviate this issue by reducing temperatures. Currently, Taiwan's urban land use zoning regulations stipulate a maximum building coverage ratio of 60% for residential areas and up to 80% for industrial and commercial zones. However, the maximum building coverage ratio for campus land is typically set at 50%, and is often lower in practice. This indicates a higher proportion of open space on campuses, presenting significant potential for the integration of small water bodies to address the cooling needs of urban areas.

This study investigated the impact of introducing small water bodies into less developed campus areas on outdoor temperature, considering the challenge of limited available space. Research methods included on-site instrumental measurements and Computational

Fluid Dynamics (CFD) simulations. The primary research objectives encompassed assessing the influence of small water bodies on surrounding temperatures, analyzing their temporal and spatial distribution of impact, and comparing instrumental measurements with software simulations. The findings of this study can offer valuable insights for planners and designers seeking to integrate water bodies into campus environments to enhance overall environmental quality and microclimate conditions.

2. Materials and Methods

To comprehend the impact of small water bodies in subtropical regions on campus outdoor temperatures, a university in Taichung City, Taiwan, was selected as the focal point of this study. The analysis unfolded in three distinct phases. Initially, we explored the water body's influence on outdoor temperatures across varying climatic conditions. This involved conducting Computational Fluid Dynamics (CFD) simulations for the hottest day, the coldest day, and an average day based on Typical Meteorological Year 3 (TMY3) data. Subsequently, on-site instrumental measurements were carried out. Over three consecutive days, specifically, from 20–22 June 2020 (Days 1 to 3), which included the summer solstice, we synchronized on-site measurements with CFD simulations. This comprehensive approach encompassed multiple measurement points at varying distances and orientations, spanning a total of 72 h. Lastly, we compared the measured data with simulation results, assessing the potential of CFD simulations in predicting the water body's temperature regulation effects on the surrounding campus area. The ensuing section provides a detailed exposition of the research methodologies employed in this investigation.

2.1. Study Area

The study area is situated in Taichung City, central Taiwan, at a longitude of $120^{\circ}42'$ E and a latitude of $24^{\circ}8'$ N, falling within the subtropical climate zone. Our focus is a university campus covering approximately 32 hectares. A detention pond, constructed in 2019, serves as our sample water body. Spanning roughly 100 m in length and 70 m in width, with a water depth ranging from 1.5 to 2.0 m, it occupies a total area of about 7150 square meters on the southwest corner of the campus. Adjacent to the pond, its northern boundary comprises open grassland, while student dormitories and teaching buildings flank its western and southern sides, with dense forest to the east. Refer to Figure 1 for the location and current condition images of the study's domain range.

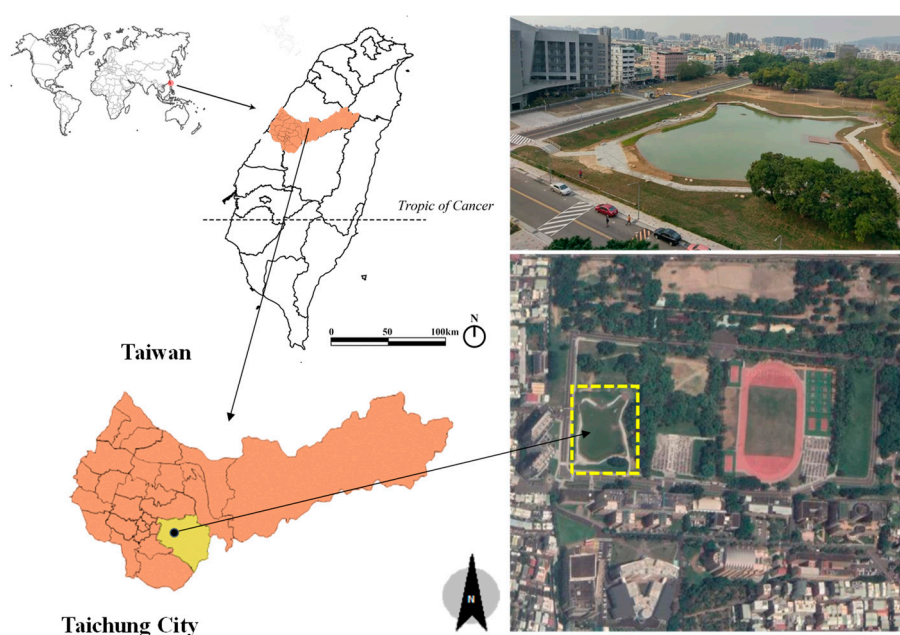


Figure 1. Study area.

2.2. Typical Meteorological Year Data

Two primary sources of meteorological data were utilized as follows: Typical Meteorological Year (TMY) data and on-site measurements collected from instruments. The TMY data employed in this study originate from TMY3 [38], compiled by Taiwan's Architecture and Building Research Institute (ABRI) of the Ministry of Internal Affairs. Derived from 23 years of data spanning 1990 to 2012, this dataset provides a comprehensive representation of local climatic conditions. After importing the TMY3 data for Taichung City into the Autodesk Ecotect Weather Tool, an analysis revealed 6 July as the hottest day, 19 February as the coldest, and 21 March as the day with the highest average temperature. Refer to Table 1 for the temperature and GHI (Global Horizontal Irradiance) of TMY data utilized in this study.

Table 1. Typical Meteorological Year data of Taichung city.

■ Time	02:00	06:00	10:00	14:00	18:00	22:00
Hottest day (6 July)						
■ Temperature (°C)	28.6	28.5	32.1	34.0	31.6	29.4
■ Global Horizontal Irradiation (W/m ²)	0	0	497	683	189	0
Coldest day (19 February)						
■ Temperature (°C)	9.8	9.8	10.4	11.7	11.2	11.3
■ Global Horizontal Irradiation (W/m ²)	0	0	97	156	0	0
Average day (21 March)						
■ Temperature (°C)	14.3	15.3	20.9	23.7	20.8	18.7
■ Global Horizontal Irradiation (W/m ²)	0	0	544	792	58	0

2.3. Instrumental Measurement

For instrumental measurement, this study employed two systems. The first system comprised Testo 480 and SPM-1116SD to record reference climate parameters of the environmental background. The second system utilized self-developed LoRa IoT Sensor Nodes, consisting of sensor hardware and real-time monitoring software, to measure the influence range around the water body. Both systems were positioned at a height of 1.6 m above ground level, corresponding to pedestrian-level wind.

2.3.1. Instrumental Measurement of Environmental Background

Testo 480 and SPM-1116SD were deployed to capture background temperature and GHI data. Positioned approximately 350 m from the sample water body to minimize its impact on measurements, Testo 480 recorded air temperature, and SPM-1116SD recorded GHI data. The sampling interval was every 10 min, and collected values were averaged once per hour. These parameters served as reference climate data for the environmental background. Please refer to Table 2 and Figure 2 for the relevant information regarding these two instruments.

Table 2. Measuring range of Testo 480 and SPM-1116SD.

Environmental Parameter	Measuring Range
Air temperature	−20 to +70 °C
Global Horizontal Irradiation (GHI)	0 to 2000 W/m ²



Testo 480



SPM-1116SD

Figure 2. Instrumental measurement of environmental background.

2.3.2. Measurement of Environmental Temperature around the Water body

To measure the environmental temperature around the sample water body, we utilized self-developed LoRa IoT Sensor Nodes as measuring devices. These nodes transmitted measured data to a computer server via the campus Wi-Fi system, where real-time temperature and relative humidity readings from each measurement point were displayed using monitoring software. Figure 3 depicts images of the hardware and real-time monitoring software for the LoRa IoT Sensor Nodes.



Node_01 狀態: Close 溫度: 27.30 濕度: 66.90	Node_02 狀態: Open 溫度: 27.30 濕度: 66.90	Node_03 狀態: Open 溫度: 27.30 濕度: 63.80
Node_04 狀態: Open 溫度: 26.70 濕度: 69.30	Node_05 狀態: Open 溫度: 27.10 濕度: 65.90	Node_06 狀態: Open 溫度: 27.50 濕度: 68.00
Node_07 狀態: Open 溫度: 27.10 濕度: 86.90	Node_08 狀態: Open 溫度: 27.50 濕度: 67.80	Node_09 狀態: Close 溫度: 濕度:
Node_10 狀態: Open 溫度: 27.20 濕度: 63.20	Node_11 狀態: Close 溫度: 濕度:	Node_12 狀態: Open 溫度: 28.30 濕度: 63.90
Node_13 狀態: Open 溫度: 26.90 濕度: 60.40	Node_14 狀態: Open 溫度: 27.20 濕度: 65.30	Node_15 狀態: Open 溫度: 27.20 濕度: 64.60

Figure 3. LoRa IoT Sensor Nodes. 狀態: mode; 溫度: temperature; 濕度: humidity.

For setting measurement points, we established four fixed points north, west, and south of the sample water body. To account for the influence of forest coverage, no measurement points were placed in the dense forest to the east. Measurement points were positioned at 10 m, 20 m, 40 m, and 80 m from the water body's edge, totaling 12 points. The height setting was consistent with the aforementioned environmental background instruments at 1.6 m. Each measurement point was numbered for ease of subsequent analysis. Figure 4 illustrates the distribution of measurement points along with on-site photographs.

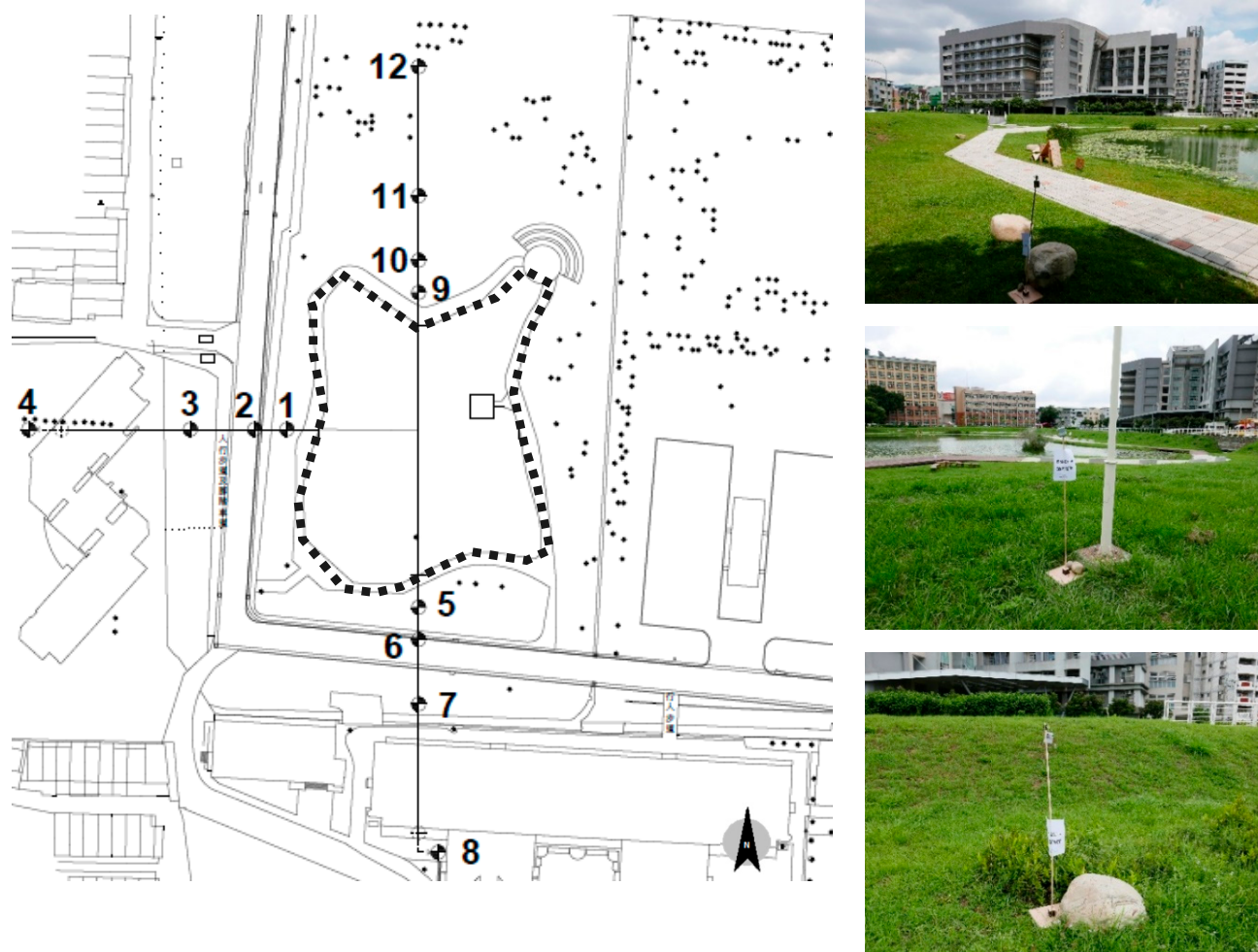


Figure 4. Distribution of measurement points. (The numbers represent the points of the locations marked for the experiment).

2.4. Computational Fluid Dynamics (CFD) Simulation in Urban Microclimate Analysis

2.4.1. Simulation Software

With recent technological advancements, various Computational Fluid Dynamics (CFD) simulation software options have emerged globally, expanding the scope of numerical simulations. CFD simulation software enables the prediction of future environmental climate changes by configuring initial conditions and climate data. In this study, we utilized ENVI-met 4.5, a specialized software for studying urban microclimates. ENVI-met emphasizes the intricate interplay between surfaces, the atmosphere, and vegetation in urban environments. It offers a wide array of analytical functions, including solar radiation analysis, air pollution dispersion, wind environment assessment, thermal comfort evaluation, and vegetation–microclimate interactions. According to a previous study [39], ENVI-met was utilized in 86 out of 177 CFD-related studies conducted from 1998 to 2015, comprising 49% of the published studies. After careful assessment of its applicability scope and referencing previous relevant research cases, this study confirmed the utilization of the CFD software, ENVI-met. ENVI-met can comprehensively analyze the impacts around buildings on campus and possible wake zones. The only available model within ENVI-met, the YMEE model (Yamada and Mellor E- ϵ), was adopted for the turbulence model in this study.

2.4.2. Turbulence Models

In practical scenarios, most gas flows exhibit turbulent behavior. Turbulence, characterized by eddies and high diffusion, poses challenges for accurate determination in calculations. Hence, selecting an appropriate turbulence model requires considering its analogical capability and computational resource demands. Among the available options, the YMEE turbulence model stands out as the sole turbulence model compatible with ENVI-met. Consequently, we employed the YMEE model in this study for turbulence simulation.

The YMEE model is a modification of the standard k - ϵ model proposed by Launder and Spalding in 1974 [40]. The standard k - ϵ model primarily discusses the turbulence kinetic energy (k) and the kinetic energy dissipation rate (ϵ). In a turbulence field, the scale of the large eddy ℓ should be related to the turbulence kinetic energy k and the kinetic energy dissipation rate ϵ :

$$\ell = \frac{k^{\frac{3}{2}}}{\epsilon} \quad (1)$$

where parameter ℓ represents the large eddy scale, k represents the turbulence kinetic energy, and ϵ represents the kinetic energy dissipation rate.

Turbulence viscosity coefficient is a function of turbulence kinetic energy k and the kinetic energy dissipation rate:

$$V_T = C_\mu \frac{k^2}{\epsilon} \quad (2)$$

where V_T is the viscosity coefficient, C_μ represents the model constant, k represents the turbulence kinetic energy, and ϵ represents the kinetic energy dissipation rate.

The larger the turbulence kinetic energy, or the smaller the kinetic energy dissipation rate, the larger the turbulence viscosity coefficient V_T . The standard k - ϵ model also contains the governing equations for turbulence kinetic energy and the kinetic energy dissipation rate:

$$\frac{\partial \bar{U}_i}{\partial x_i} = 0 \quad (3)$$

$$\frac{D\bar{U}_i}{Dt} = -\frac{1}{\rho} \frac{\partial \bar{P}}{\partial x_i} + v_T \nabla^2 \bar{U}_i \quad (4)$$

$$\frac{Dk}{Dt} = \frac{\partial}{\partial x_i} \left(\frac{V_T}{C_k} \cdot \frac{\partial k}{\partial x_i} \right) + v_t \left(\frac{\partial \bar{U}_i}{\partial x_j} + \frac{\partial \bar{U}_j}{\partial x_i} \right) \cdot \frac{\partial \bar{U}_i}{\partial x_j} - \epsilon \quad (5)$$

$$\frac{D\epsilon}{Dt} = \frac{\partial}{\partial x_i} \left(\frac{V_T}{C_\epsilon} \cdot \frac{\partial \epsilon}{\partial x_i} \right) + c_{1\epsilon} \frac{\epsilon}{k} V_T \left(\frac{\partial \bar{U}_i}{\partial x_j} + \frac{\partial \bar{U}_j}{\partial x_i} \right) \cdot \frac{\partial \bar{U}_i}{\partial x_j} - c_{2\epsilon} \frac{\epsilon^2}{k} \quad (6)$$

where the model constant $C_\mu = 0.09$, $C_{1\epsilon} = 1.44$, $C_{2\epsilon} = 1.92$, $C_k = 1.0$, and $C_\epsilon = 1.3$, all of which are obtained by comparing the experimental data results with the model calculation.

The YMEE model was established based on the research of Mellor and Yamada in 1975 [41]. In the standard k - ϵ model, two additional formulas were added to calculate turbulence (E) and dissipation (ϵ), respectively:

$$\frac{\partial E}{\partial t} + u_i \frac{\partial E}{\partial x_i} = k_E \left(\frac{\partial^2 E}{\partial x_i^2} \right) + P_r - Th + Q_E - \epsilon \quad (7)$$

$$\frac{\partial \epsilon}{\partial t} + u_i \frac{\partial \epsilon}{\partial x_i} = k_\epsilon \left(\frac{\partial^2 \epsilon}{\partial x_i^2} \right) + c_{1\epsilon} \frac{\epsilon}{E} Pr - c_{2\epsilon} \frac{\epsilon}{E} Th - c_{3\epsilon} \frac{\epsilon^2}{E} + Q_\epsilon \quad (8)$$

where c_1 , c_2 , and c_3 are empirical constants, whose values are taken from the studies of Launder and Spalding [40]. $c_1 = 1.44$; $c_2 = 1.92$; and $c_3 = 1.44$.

Pr and Th represent the generation and dissipation of turbulence energy due to wind shearing and thermal stratification based on the following formulas:

$$\text{Pr} = k_m \left(\frac{\partial u_i}{\partial x_j} \frac{\partial u_j}{\partial z_i} \right) \frac{\partial u_i}{\partial x_j} \quad (9)$$

$$\text{Th} = \frac{g}{\theta_{\text{ref}}(Z)} K h \frac{\partial \theta}{\partial z} \quad (10)$$

where $\theta_{\text{ref}}(z)$ indicates the potential temperature at the boundary at a particular height. Under stable conditions, Th is negligible.

2.4.3. Domain Range and Grid Size

In CFD simulation, the height (H) of the tallest building within the region often serves as a reference for defining the domain range size [42]. Drawing from Franke et al. [43], this study adopted initial guidelines for calculating the domain range size. Franke et al. recommended positioning the side and top boundaries of the building 5 H away from the building in the direction of the wind inlet, while the rear boundary should extend at least 15 H behind the building to ensure stable airflow.

This study adopted a height (H) of 21 m, corresponding to the height of the tallest building, as the basis for calculation. The domain range height was determined as 126 m, equivalent to six times the height of the tallest building. To account for varying wind directions in the simulation, a distance of 15 H was established as the boundary distance in all four directions. Thus, the simulation's domain range was defined as 630 m × 630 m × 126 m. A grid size of 2 m × 2 m × 2 m was selected for each grid, resulting in a total of 6,251,175 grids. Additionally, in ENVI-met, the grid closest to the bottom of the Z-axis can be divided into five equal sections with cross-sectional heights of 0.4 m, 0.8 m, 1.2 m, 1.6 m, and 2.0 m, respectively. This study utilized cross-sectional data with a height of 1.6 m to match the height of the instrumental measurements mentioned above.

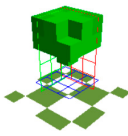
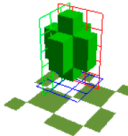
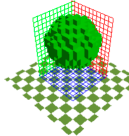
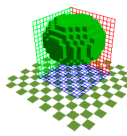
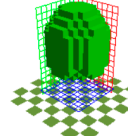
2.4.4. Setting Object Parameters

In the initial setup phase of ENVI-met, it is imperative to configure parameters for objects within the domain range under examination. This study focused on three primary components: ground materials, vegetation, and buildings. Upon investigation, campus ground materials were categorized into asphalt pavement, permeable brick, concrete pavement, soil, and water. Definitions used in the initial setup of ENVI-met are detailed in Table 3. Various types of plants populate the campus, with this study selecting and categorizing large trees into five types: *Ficus microcarpa*, *Koelreuteria elegans*, *Mangifera indica*, the camphor tree, and the mahogany tree. Parameters for different tree species were adjusted using the *Albero* module of ENVI-met, as outlined in Table 4. Additionally, ENVI-met's built-in turf parameters were utilized and adjusted to match the campus turf height of 0.2 m. For modeling campus buildings, the built-in concrete building feature of ENVI-met was employed, with each floor set at a height of 3 m.

Table 3. Definitions of ground materials in ENVI-met.

Ground Materials	Asphalt	Permeable Brick	Concrete Pavement	Soil	Water
Photograph					
Material setting identification number	[0100ST] Asphalt Road	[0100PP] Pavement	[0100PG] Concrete Pavement Gray	[0100LO] Loamy Soil	[0100WW] Deep Water

Table 4. Parameters for different tree species in ENVI-met.

Species	Ficus Microcarpa	Koelreuteria Formosana	Mangifera Indica	Cinnamomum Camphora	Swietenia Mahagoni
Photograph					
Height	5 m	5 m	10 m	15 m	15 m
Tree species name in ENVI-met	Heart-shaped, small trunk	Spherical, small trunk	Spherical, medium trunk	Heart-shaped, medium trunk	Cylindric
Tree models in ENVI-met					

2.4.5. Simulation Time Interval

Given computational constraints, this study adopted a simulation time interval of every four hours: 02:00, 06:00, 10:00, 14:00, 18:00, and 22:00. The influence of water bodies on the outdoor temperature of the campus was assessed through data sampling points collected at these six time intervals.

3. Results of Numerical Simulation on Surrounding Environmental Temperature

The numerical simulations in this study were divided into two parts based on different objectives. The first part focused on investigating the influence of small water bodies on the surrounding environmental temperatures at different times. Based on Typical Meteorological Year (TMY) data in the study area, numerical simulations were conducted for the hottest day (6 July), coldest day (19 February), and a day with average temperatures (21 March). Figure 5 presents excerpts of the results of numerical simulation partly. The purpose of the second part was to compare the temperature differences between numerical simulations and instrumental measurements. Numerical simulations were conducted over three consecutive days (72 h) encompassing the summer solstice in 2020 and the days immediately before and after, namely 20–22 June (Day 1 to Day 3). Figure 6 presents the variations in the surrounding environmental temperature on Day 2. Subsequently, we will couple this with instrumental measurements to explore the feasibility of using numerical simulations to predict actual temperature distributions.

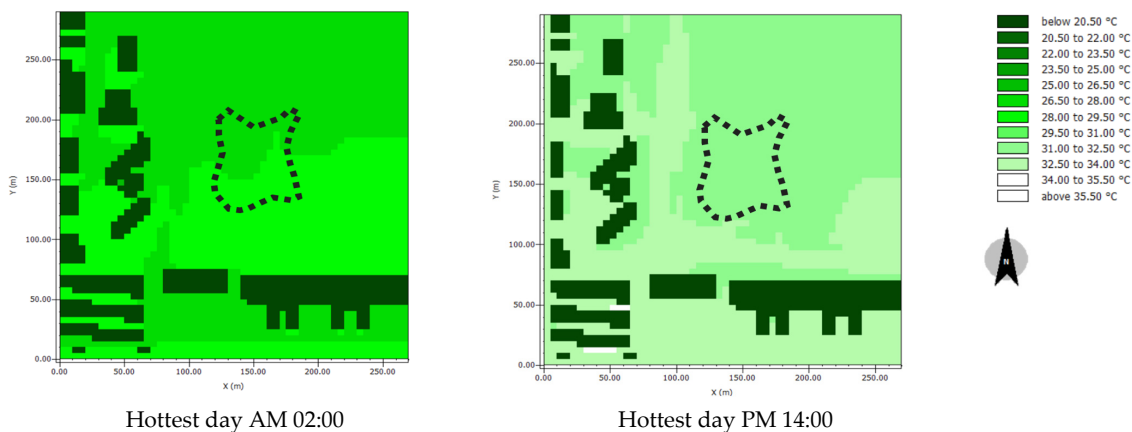


Figure 5. Cont.

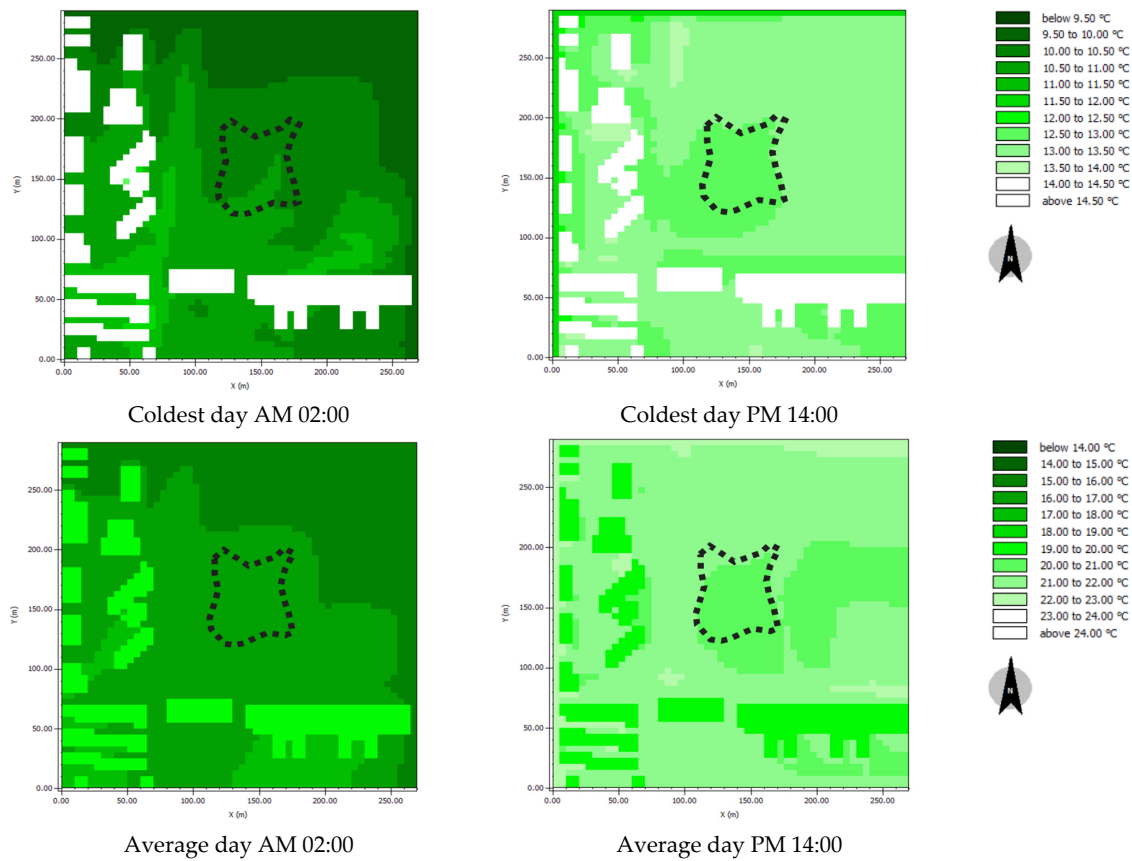


Figure 5. Results of numerical simulation on the surrounding environmental temperatures based on TMY data (partly).

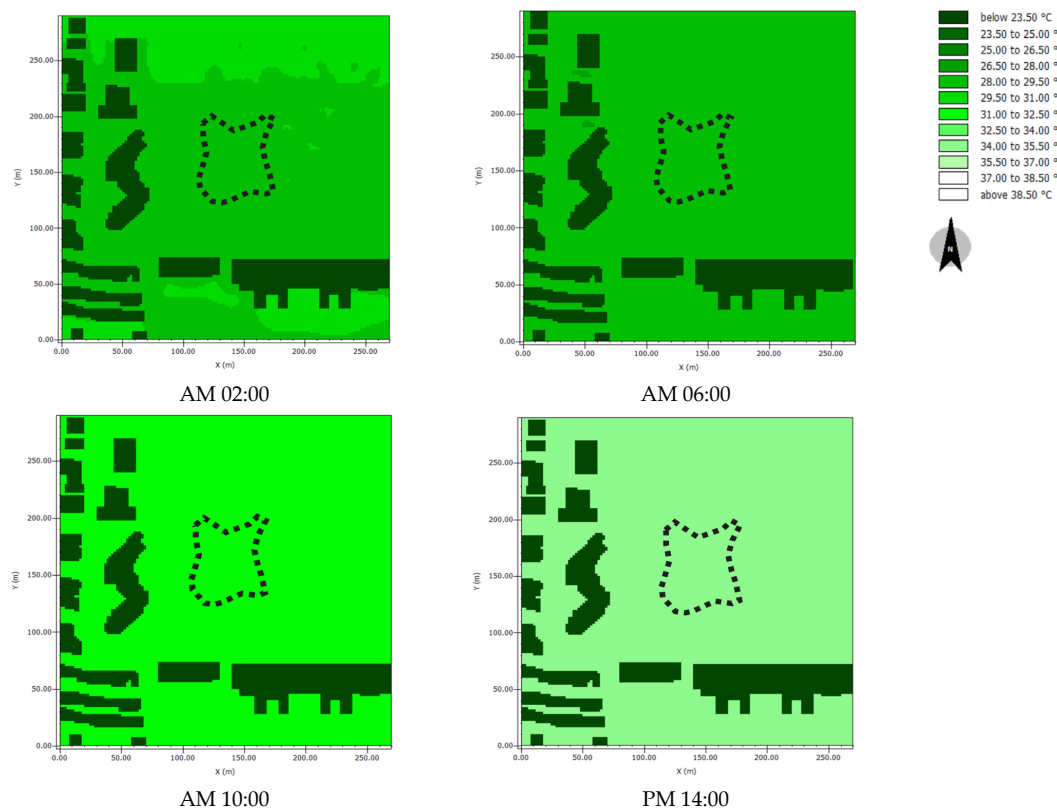


Figure 6. Cont.

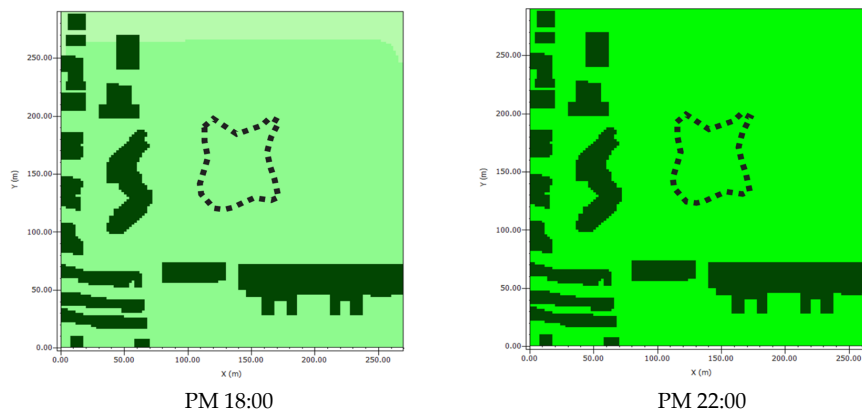


Figure 6. Results of numerical simulation on the surrounding environmental temperature variations on Day 2 (21 June 2020).

4. ENVI-Met Simulation Results and Coupling with Measurement Data

In this section, we compared temperature distribution values at a cross-sectional height of 1.6 m, derived from the ENVI-met simulation results. Positioned on the north, west, and south sides of the sample water body, these points were located at distances of 10 m, 20 m, 40 m, and 80 m from the sample water body, respectively. Afterward, we utilized data collected from environmental measuring instruments positioned 350 m away from the sample water body as background values, coupled with the ENVI-met simulation results. This coupling served as the reference basis for predicting temperature variations due to the influence of small water bodies.

4.1. ENVI-met Simulation Results

4.1.1. The Hottest Day of TMY3

Figure 7 illustrates the comparison results of numerical simulations on the hottest day based on TMY3 data. The background reference temperatures for that day were 28.5 °C at 06:00 (minimum) and 34.0 °C at 14:00 (maximum). Due to the temperature regulation function of the water body, all surrounding areas experienced a certain degree of temperature reduction. The largest temperature drop, 1.8 °C, occurred at 14:00, while the smallest drop, 0.6 °C, was observed at 22:00. This variance can be attributed to the substantial amount of Global Horizontal Irradiation (GHI) received during the day compared to none being received at night. Interestingly, the distance between measurement points and the water body had minimal impact on temperature, with differences ranging only between 0.2 °C and 0.4 °C, showing no significant variation.

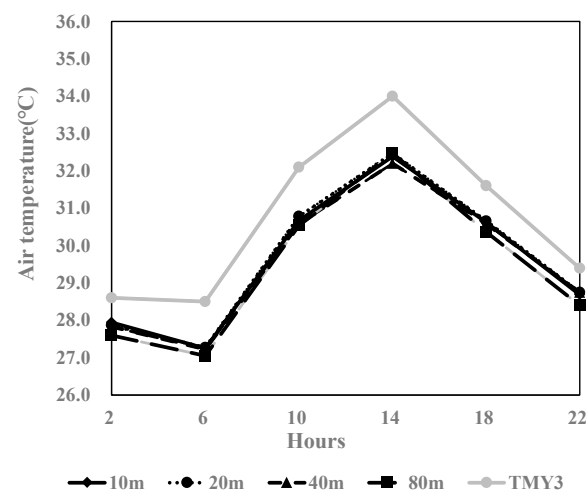


Figure 7. Comparison results of numerical simulations (I) (hottest day of TMY3).

4.1.2. The Coldest Day of TMY3

Figure 8 presents the comparison results of numerical simulations on the coldest day based on TMY3 data. On this day, background reference temperatures were recorded as 9.8 °C at 02:00 (minimum) and 11.7 °C at 14:00 (maximum). The water body's temperature regulation function led to a degree of temperature increase in all surrounding areas. The largest temperature rise, 3.9 °C, occurred at 10:00, while the smallest rise, 0.1 °C, was observed at 22:00. This pattern is primarily influenced by the significant amount of GHI received during the day. Notably, the impact of distance on temperature varied: when GHI was higher, the distance between measurement points and the water body exerted a more pronounced effect. For instance, at 10:00, temperatures were 3.2 °C, 3.5 °C, 3.9 °C, and 2.3 °C higher than the TMY3 background temperature at distances of 10 m, 20 m, 40 m, and 80 m, respectively. Conversely, during periods of low GHI or at night, the distance's impact was relatively minor, with temperature differences between distances ranging from 0.1 °C to 1.6 °C.

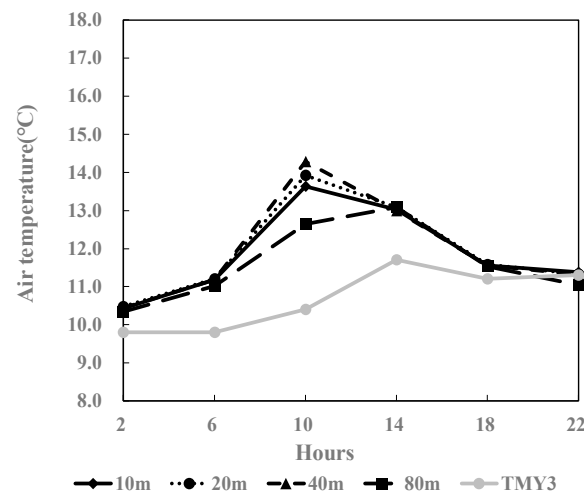


Figure 8. Comparison results of numerical simulations (II) (coldest day of TMY3).

4.1.3. The Day with an Average Temperature of TMY3

Figure 9 displays the comparison results of numerical simulations for the day with an average temperature based on TMY3 data. On this day, the background reference temperatures were recorded as 14.3 °C at 02:00 (minimum) and 23.7 °C at 14:00 (maximum). The impact of distance between measurement points and the water body on temperature can be categorized into four stages.

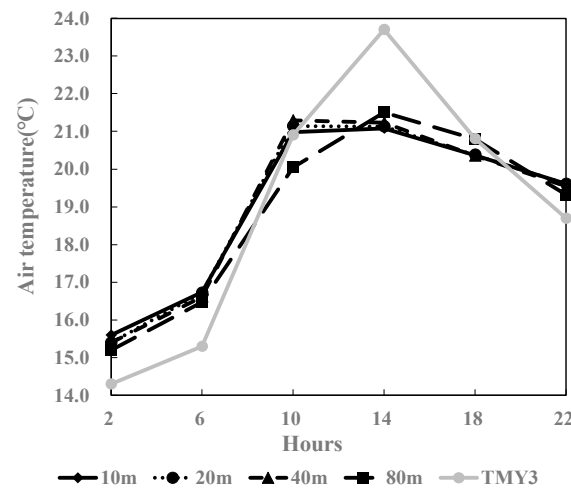


Figure 9. Comparison results of numerical simulations (III) (average day of TMY3).

In the first stage, between 02:00 and 06:00 when GHI was 0, the surrounding areas experienced a temperature rise to some extent, ranging from approximately 0.9 °C to 1.4 °C. The temperature difference between different distances ranged from 0.3 °C to 0.4 °C. The second stage occurred at 10:00, when temperatures began to rise with the increase in Global Horizontal Irradiation. The water body absorbed radiant heat, mitigating the temperature rise of the surrounding areas. During this period, temperatures around the water body were approximately 0.1 °C to 0.4 °C higher than the TMY3 background temperature, except for the point 80 m away, which was 0.9 °C lower. The third stage, at 14:00, showcased the water body's optimal cooling effect, with a maximum temperature drop of 2.6 °C. However, the distance from the water body had minimal impact on temperature, with differences between distances ranging from only 0.1 °C to 0.4 °C. The fourth stage, at 18:00, saw temperatures begin to drop. The water body released radiant heat, slowing the temperature decrease in the surrounding areas. Temperatures during this period were approximately 0.3 °C to 0.4 °C lower than the TMY3 background temperature, except for the point 80 m away, which was 0.1 °C higher. In the final stage, as GHI dropped to 0, the surrounding areas experienced a temperature rise, ranging from approximately 0.6 °C to 0.9 °C. The temperature difference between different distances ranged from 0.1 °C to 0.3 °C.

Compared to previous studies, the cooling effect of water bodies manifests differently in diurnal and spatial variations, influenced by changes in Global Horizontal Irradiation (GHI). This leads to inconsistent cooling effects between day and night [30]. Additionally, in winter, the domain range around the water body may experience significant temperature increases during the day, while the water body's temperature regulation effect at night diminishes, correlating with the amount of received GHI. However, regarding the water body's impact on temperature in the surrounding domain range, there is no clear indication that its regulation effect decreases with distance, potentially constrained by the water body's size.

4.2. Coupling with Measurement Data

4.2.1. CFD Simulation Results

Figure 10 illustrates the simulation of the water body's impact on the outdoor temperature of the surrounding domain range over three days: 20 June 2020–22 June 2020 (Day 1–Day 3). Regarding the background reference temperature at a point 350 m away from the water body, the highest temperature was recorded at 38.6 °C at 14:00 on Day 2, followed by 37.5 °C at 10:00 on Day 3. Conversely, the lowest temperatures occurred at 26.5 °C at 02:00 on the night of Day 1 and 27.0 °C at 02:00 on the night of Day 2. The CFD simulation results mirrored those of the hottest day of TMY3, as depicted in Figure 7. During the daytime, the surrounding domain range of the sample water body experienced a notable temperature drop. Specifically, the largest temperature drop, reaching 3.5 °C, was observed at 14:00 on Day 2, followed by 2.6 °C at 10:00 on Day 2. Conversely, at night, the temperature drop values tended to diminish, with most nights registering drops below 0.6 °C, even exhibiting slight temperature rises. Notably, except for a temperature drop of 1.0 °C at 02:00 on the night of Day 3, all other nights saw drops below 0.6 °C. The distance from the water body exhibited minimal impact on temperature, with variations of only 0.1–0.7 °C between different distances. Notably, there were no significant differences observed. This outcome aligns with the simulation results of the hottest day of TMY3, as illustrated in Figure 7.

4.2.2. Evaluation of Outdoor Temperature Surrounding the Water Body

Figure 11 illustrates the recorded temperature values at various measurement points surrounding the water body across three consecutive days: from 20 June 2020 to 22 June 2020 (designated as Day 1 to Day 3). Throughout the daytime, a discernible temperature drop was observed in the vicinity of the water body. The most significant temperature drop occurred at 10:00 on Day 2, registering a decrease of 3.2 °C, followed by a drop of 2.9 °C at 14:00 on the same day. During the night, temperature drops tended to diminish,

ranging between 0.3 to 1.3 °C, occasionally exhibiting slight increments. These observations highlight notable variations in simulation outcomes, underscoring the influential role of distance between measurement points and the water body in temperature fluctuation.

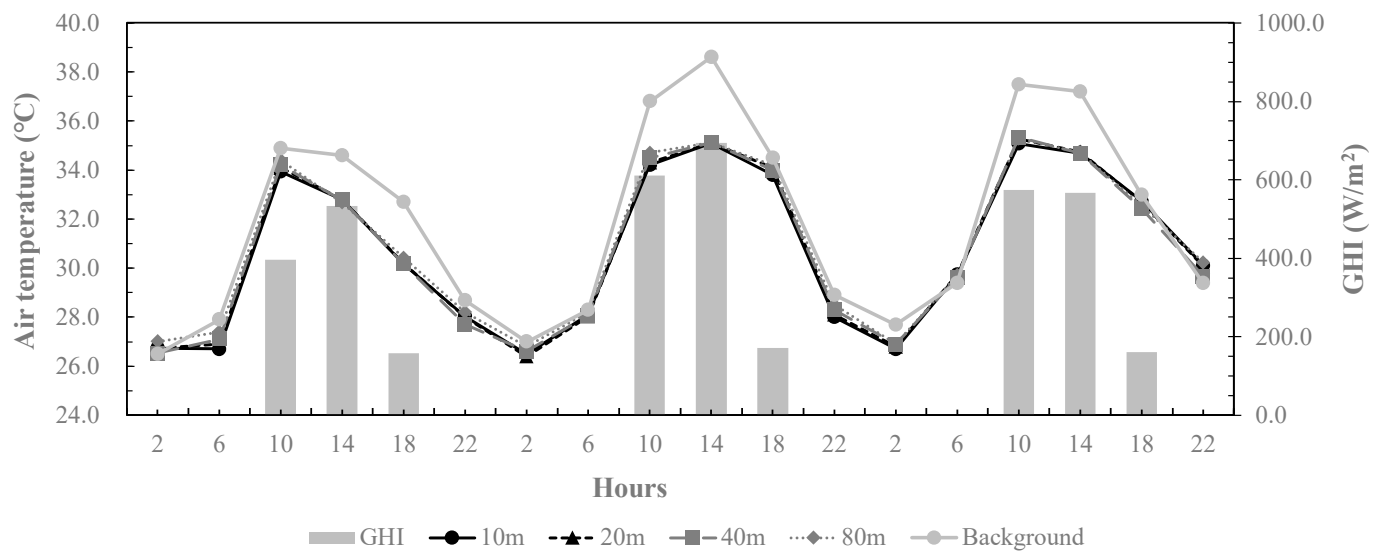


Figure 10. Simulation of the water body's impact on the outdoor temperature.

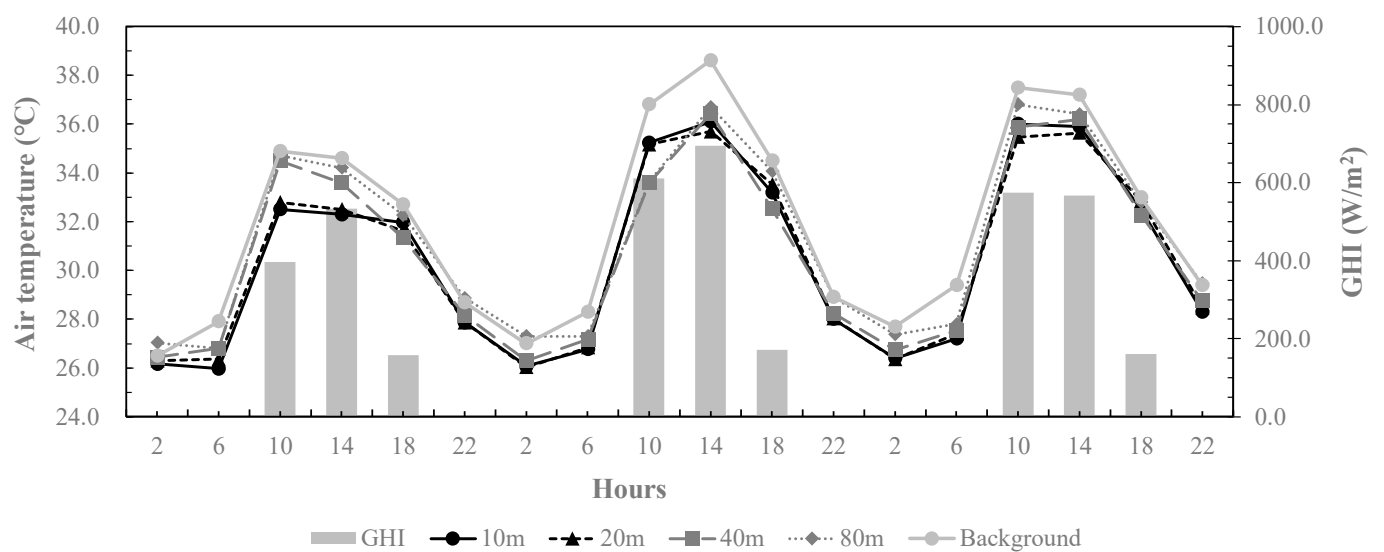


Figure 11. Temperature values of measurement points surrounding the water body.

For instance, at 10:00 on Day 1, temperatures recorded at distances of 10 m, 20 m, 40 m, and 80 m were, respectively, 2.4 °C, 2.1 °C, 0.4 °C, and 0.2 °C lower than the background reference temperature observed at a distance of 350 m. Similarly, at 14:00 on Day 2, temperatures at the same distances were 2.5 °C, 2.9 °C, 2.2 °C, and 2.1 °C lower compared to the reference temperature at 350 m. Conversely, during the night-time at 02:00 on Day 2, temperatures at distances of 10 m, 20 m, 40 m, and 80 m were 0.9 °C, 1.0 °C, and 0.7 °C lower, and 0.3 °C higher, respectively, than the reference temperature at 350 m.

4.2.3. Comparative Analysis of Simulations and Measurement Results

Figure 12 juxtaposes the deviation values between simulation and measurement results obtained from Computational Fluid Dynamics (CFD) simulations (Figure 10) and instrumental measurements (Figure 11). These deviation values range from +2.5 °C to −1.8 °C. An analysis reveals that during late night and early morning hours, simulated

values tended to exceed measured values, with the largest deviation occurring between 06:00 and 10:00 in the morning. Conversely, during the afternoon, measured values surpassed simulated values, reaching peak deviation between 14:00 and 18:00. Notably, the study observed that when Global Horizontal Irradiance (GHI) values were high during the day, measured values exceeded simulated values. Conversely, during the night when GHI values were low or zero, simulated values surpassed measured values.

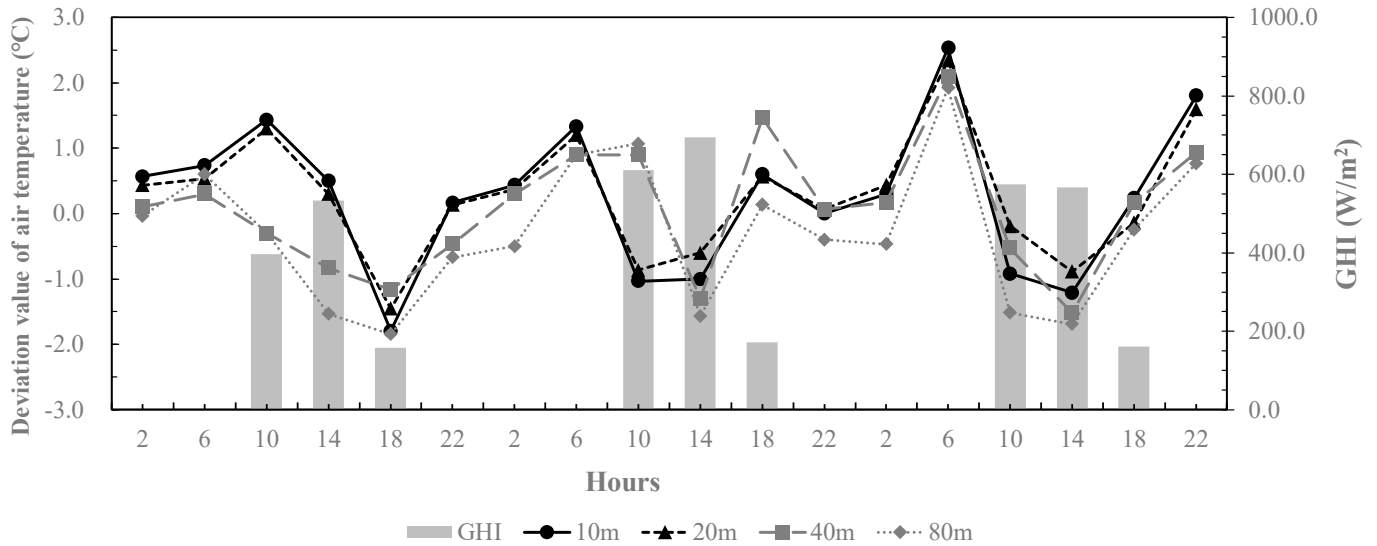


Figure 12. Deviation values between simulation and measurement results.

A comparative analysis between simulations and instrumental measurements was conducted over 3 days (20 June 2020–22 June 2020), with data intervals of 4 h. A total of 18 sets of data were utilized for comparisons. Figure 13 presents a regression analysis diagram correlating values derived from CFD simulations and instrumental measurements at various distances from the water body. The coefficient of determination (R^2) ranged from 0.9250 to 0.9435, indicating high overall accuracy. Thus, employing CFD simulation methodology for predicting a water body’s cooling effect on surrounding temperatures is deemed feasible. The resultant regression equation can serve as a valuable reference for calibrating simulated and measured values.

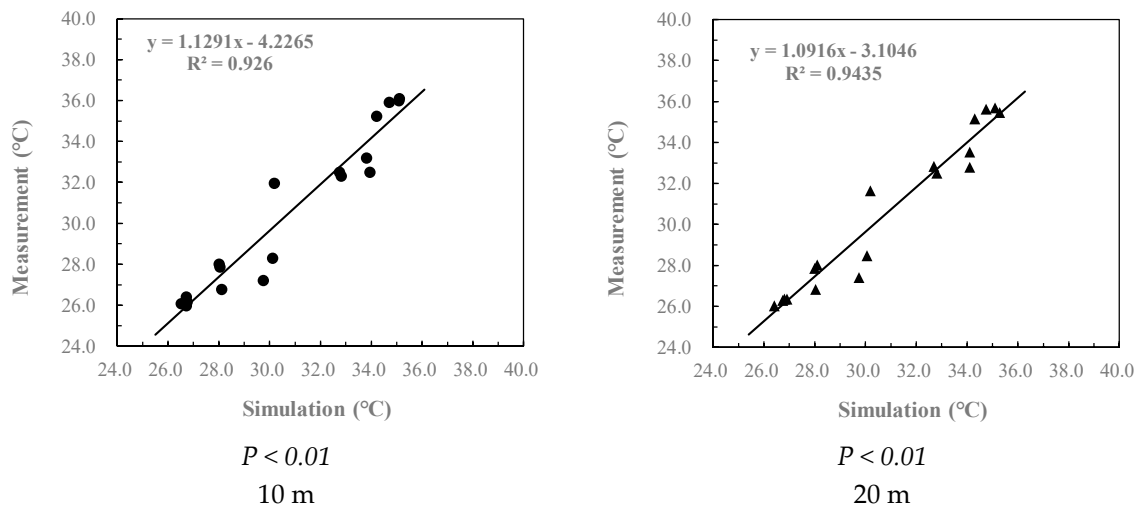
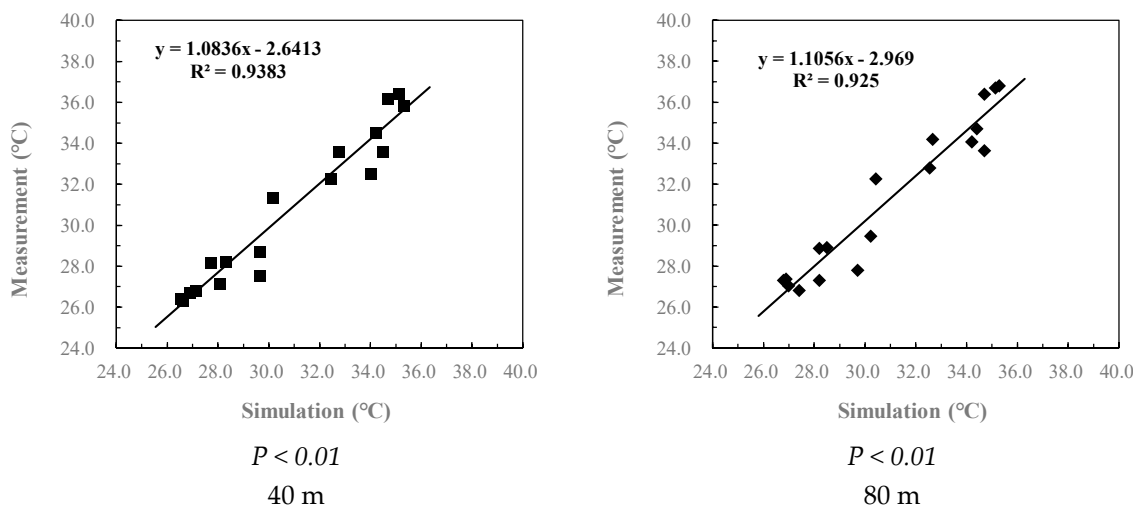


Figure 13. Cont.



These points represent XY scatter plots.

Figure 13. Regression analysis of CFD simulations and measurement results.

5. Conclusions

With the exacerbation of global warming and rapid urban development, the urban heat island effect has become increasingly severe. Consequently, outdoor thermal comfort has garnered heightened attention in the research field. Suitable outdoor thermal comfort not only enhances the utilization rate of outdoor spaces but also influences indoor thermal comfort and energy-saving endeavors to some extent. This study focused on water bodies, known for their effective cooling impact on the urban heat island effect, as the subject of investigation. Introducing the concept of distributed water body patches, this study proposed a solution for densely urbanized areas where large water bodies may not be feasible. By strategically placing small water bodies in campuses with low building density, temperature reductions can be achieved. Integrating water bodies into campus landscape planning has the potential to create favorable microclimates and enhance overall campus environments. Future endeavors should extend this approach to urban areas to combat the urban heat island effect effectively, thereby improving outdoor thermal comfort and reducing indoor air conditioning demands, consequently lowering urban energy consumption.

The conclusions drawn from this study are as follows:

1. Both CFD simulation and on-site measurements confirm the influence of water bodies on outdoor temperatures in the surrounding domain range. However, the decrease in the regulation effect with increasing distance from the water body is not pronounced, potentially constrained by the size of the water body patch;
2. The temperature regulation effect of water bodies varies between day and night, primarily driven by changes in Global Horizontal Irradiation (GHI). During summer, temperature drops of up to 3.5 °C (simulated) and 3.2 °C (measured) can be observed. Conversely, in winter, significant temperature rises during the day, up to 3.9 °C, are noted, while the night-time regulation effect of water bodies is minimal;
3. A comparison between CFD simulation and on-site measurement revealed deviation values influenced by fluctuations in GHI, ranging between +2.5 °C and −1.8 °C. Higher GHI values during the day result in higher measured temperatures compared to simulated values, whereas lower or zero GHI values at night lead to higher simulated temperatures than measured values. Regression analysis yielded R^2 values between 0.9250 and 0.9435, indicating relatively high overall accuracy. Thus, the CFD simulation method proves feasible for predicting water bodies' regulation effect on surrounding domain range temperatures, with the obtained regression equation serving as a reference for correcting simulated values.

This study primarily focused on the influence of small water bodies on the urban heat island phenomenon. The main factor under investigation was outdoor temperature. However, climate factors such as relative humidity, wind speed, wind direction, seasonal variations, and different climate areas were likely to affect the results. Currently, these factors are considered limitations and uncertainties of this study. Further simulations and comparisons between simulated and measured values will be conducted to progressively refine the research results and enhance the reliability of this study.

Author Contributions: Conceptualization, M.-C.L. and W.-P.S.; methodology, M.-C.L. and W.-P.S.; software, M.-C.L. and Q.-Q.C.S.; validation, M.-C.L.; formal analysis, M.-C.L. and W.-P.S.; investigation, Q.-Q.C.S.; data curation, Q.-Q.C.S.; writing—original draft preparation, M.-C.L. and W.-P.S.; writing—review and editing, M.-C.L. and W.-P.S.; visualization, M.-C.L. All authors have read and agreed to the published version of the manuscript.

Funding: This research was funded by the National Science and Technology Council, Taiwan, through grant No. NSTC 112-2410-H-167-011.

Data Availability Statement: No new data were created or analyzed in this study.

Conflicts of Interest: The authors declare no conflict of interest.

References

- Rosatto, H.; Botta, G.F.; Becerra, A.T.; Tardito, H.; Leveratto, M. Climate change difficulties in the buenos aires city contribution of green roofs in regulating the thermal change. *Rev. Fac. Cienc. Agrar.* **2016**, *48*, 197–209.
- Oke, T.R. The energetic basis of the urban heat island. *Q. J. R. Meteorol. Soc.* **1982**, *108*, 1–24. [[CrossRef](#)]
- Voogt, J.A.; Oke, T.R. Thermal remote sensing of urban climates. *Remote Sens. Environ.* **2003**, *86*, 370–384. [[CrossRef](#)]
- Mills, G.; Cleugh, H.; Emmanuel, R.; Endlicher, W.; Erell, E.; McGranahan, G.; Ng, E.; Nickson, A.; Rosenthal, J.; Steemer, K. Climate Information for Improved Planning and Management of Mega Cities (Needs Perspective). *Procedia Environ. Sci.* **2010**, *1*, 228–246. [[CrossRef](#)]
- IPCC—Intergovernmental Panel on Climate Change. Long-term Climate Change: Projections, Commitments and Irreversibility. In *Climate Change 2013—The Physical Science Basis: Working Group I Contribution to the Fifth Assessment Report of the Intergovernmental Panel on Climate Change*; Intergovernmental Panel on Climate Change, Ed.; Cambridge University Press: Cambridge, UK, 2014; pp. 1029–1136.
- Akbari, H.; Matthews, H.D.; Seto, D. The long-term effect of increasing the albedo of urban areas. *Environ. Res. Lett.* **2012**, *7*, 024004. [[CrossRef](#)]
- Cartalis, C.; Synodinou, A.; Proedrou, M.; Tsangrassoulis, A.; Santamouris, M. Modifications in energy demand in urban areas as a result of climate changes: An assessment for the southeast Mediterranean region. *Energy Convers. Manag.* **2001**, *42*, 1647–1656. [[CrossRef](#)]
- Kolokotroni, M.; Ren, X.; Davies, M.; Mavrogianni, A. London’s urban heat island: Impact on current and future energy consumption in office buildings. *Energy Build.* **2012**, *47*, 302–311. [[CrossRef](#)]
- He, X.; Wang, J.; Feng, J.; Yan, Z.; Miao, S.; Zhang, Y.; Xia, J. Observational and modeling study of interactions between urban heat island and heatwave in Beijing. *J. Clean. Prod.* **2020**, *247*, 119169. [[CrossRef](#)]
- Li, D.; Bou-Zeid, E. Synergistic Interactions between Urban Heat Islands and Heat Waves: The Impact in Cities Is Larger than the Sum of Its Parts. *J. Appl. Meteorol. Clim.* **2013**, *52*, 2051–2064. [[CrossRef](#)]
- Ramamurthy, P.; Bou-Zeid, E. Heatwaves and urban heat islands: A comparative analysis of multiple cities. *J. Geophys. Res. Atmos.* **2017**, *122*, 168–178. [[CrossRef](#)]
- Kotharkar, R.; Bagade, A. Evaluating urban heat island in the critical local climate zones of an Indian city. *Landsc. Urban Plan.* **2018**, *169*, 92–104. [[CrossRef](#)]
- Kotharkar, R.; Surawar, M. Land Use, Land Cover, and Population Density Impact on the Formation of Canopy Urban Heat Islands through Traverse Survey in the Nagpur Urban Area, India. *J. Urban Plan. Dev.* **2016**, *142*, 04015003. [[CrossRef](#)]
- Pyrgou, A.; Santamouris, M. Increasing Probability of Heat-Related Mortality in a Mediterranean City Due to Urban Warming. *Int. J. Environ. Res. Public Health* **2018**, *15*, 1571. [[CrossRef](#)] [[PubMed](#)]
- Klok, L.; Zwart, S.; Verhagen, H.; Mauri, E. The surface heat island of Rotterdam and its relationship with urban surface characteristics. *Resour. Conserv. Recycl.* **2012**, *64*, 23–29. [[CrossRef](#)]
- Lai, D.; Liu, W.; Gan, T.; Liu, K.; Chen, Q. A review of mitigating strategies to improve the thermal environment and thermal comfort in urban outdoor spaces. *Sci. Total Environ.* **2019**, *661*, 337–353. [[CrossRef](#)] [[PubMed](#)]
- Peng, J.; Xie, P.; Liu, Y.; Ma, J. Urban thermal environment dynamics and associated landscape pattern factors: A case study in the Beijing metropolitan region. *Remote Sens. Environ.* **2016**, *173*, 145–155. [[CrossRef](#)]
- Sun, R.; Xie, W.; Chen, L. A landscape connectivity model to quantify contributions of heat sources and sinks in urban regions. *Landsc. Urban Plan.* **2018**, *178*, 43–50. [[CrossRef](#)]

19. Costanzo, V.; Evola, G.; Marletta, L. Energy savings in buildings or UHI mitigation? Comparison between green roofs and cool roofs. *Energy Build.* **2016**, *114*, 247–255. [[CrossRef](#)]
20. Kotharkar, R.; Bagade, A.; Singh, P.R. A systematic approach for urban heat island mitigation strategies in critical local climate zones of an Indian city. *Urban Clim.* **2020**, *34*, 100701. [[CrossRef](#)]
21. Yang, G.; Yu, Z.; Jørgensen, G.; Vejre, H. How can urban blue-green space be planned for climate adaption in high-latitude cities? A seasonal perspective. *Sustain. Cities Soc.* **2020**, *53*, 101932. [[CrossRef](#)]
22. Wong, N.H.; Tan, C.L.; Nindyani AD, S.; Jusuf, S.K.; Tan, E. Influence of water bodies on outdoor air temperature in hot and humid climate. In *ICSDC 2011: Integrating Sustainability Practices in the Construction Industry, Proceedings of the 2011 International Conference*; American Society of Civil Engineers: Reston, VA, USA, 2012. [[CrossRef](#)]
23. Deilami, K.; Kamruzzaman, M.; Liu, Y. Urban heat island effect: A systematic review of spatio-temporal factors, data, methods, and mitigation measures. *Int. J. Appl. Earth Obs. Geoinf.* **2018**, *67*, 30–42. [[CrossRef](#)]
24. Hu, L.; Li, Q. Greenspace, bluespace, and their interactive influence on urban thermal environments. *Environ. Res. Lett.* **2020**, *15*, 034041. [[CrossRef](#)]
25. Brans, K.I.; Engelen, J.M.; Souffreau, C.; De Meester, L. Urban hot-tubs: Local urbanization has profound effects on average and extreme temperatures in ponds. *Landsc. Urban Plan.* **2018**, *176*, 22–29. [[CrossRef](#)]
26. Sun, R.; Chen, A.; Chen, L.; Lü, Y. Cooling effects of wetlands in an urban region: The case of Beijing. *Ecol. Indic.* **2012**, *20*, 57–64. [[CrossRef](#)]
27. Coutts, A.M.; Tapper, N.J.; Beringer, J.; Loughnan, M.; Demuzere, M. Watering our cities. *Prog. Phys. Geogr. Earth Environ.* **2012**, *37*, 2–28. [[CrossRef](#)]
28. Saaroni, H.; Ziv, B. The impact of a small lake on heat stress in a Mediterranean urban park: The case of Tel Aviv, Israel. *Int. J. Biometeorol.* **2003**, *47*, 156–165. [[CrossRef](#)] [[PubMed](#)]
29. Smith, C.; Levermore, G. Designing urban spaces and buildings to improve sustainability and quality of life in a warmer world. *Energy Policy* **2008**, *36*, 4558–4562. [[CrossRef](#)]
30. Chen, Y.-C.; Tan, C.-H.; Wei, C.; Su, Z.-W. Cooling Effect of Rivers on Metropolitan Taipei Using Remote Sensing. *Int. J. Environ. Res. Public Health* **2014**, *11*, 1195–1210. [[CrossRef](#)]
31. Hathway, E.A.; Sharples, S. The interaction of rivers and urban form in mitigating the Urban Heat Island effect: A UK case study. *Build. Environ.* **2012**, *58*, 14–22. [[CrossRef](#)]
32. Sun, R.; Chen, L. How can urban water bodies be designed for climate adaptation? *Landsc. Urban Plan.* **2012**, *105*, 27–33. [[CrossRef](#)]
33. Xue, Z.; Hou, G.; Zhang, Z.; Lyu, X.; Jiang, M.; Zou, Y.; Shen, X.; Wang, J.; Liu, X. Quantifying the cooling-effects of urban and peri-urban wetlands using remote sensing data: Case study of cities of Northeast China. *Landsc. Urban Plan.* **2019**, *182*, 92–100. [[CrossRef](#)]
34. Moyer, A.N.; Hawkins, T.W. River effects on the heat island of a small urban area. *Urban Clim.* **2017**, *21*, 262–277. [[CrossRef](#)]
35. Cai, Z.; Han, G.; Chen, M. Do water bodies play an important role in the relationship between urban form and land surface temperature? *Sustain. Cities Soc.* **2018**, *39*, 487–498. [[CrossRef](#)]
36. Du, H.; Song, X.; Jiang, H.; Kan, Z.; Wang, Z.; Cai, Y. Research on the cooling island effects of water body: A case study of Shanghai, China. *Ecol. Indic.* **2016**, *67*, 31–38. [[CrossRef](#)]
37. Yu, Z.; Yang, G.; Zuo, S.; Jørgensen, G.; Koga, M.; Vejre, H. Critical review on the cooling effect of urban blue-green space: A threshold-size perspective. *Urban For. Urban Green.* **2020**, *49*, 126630. [[CrossRef](#)]
38. He, M.J.; Huang, G.C.; Wang, R.J.; Yu, W.Y.; Lin, J.S. *Establishment and Research of TMY3 Hourly Standard Weather Data for Building Energy Simulation Analysis in Taiwan*; Architecture and Building Research Institute, Ministry of the Interior: Taiwan, China, 2013.
39. Toparlar, Y.; Blocken, B.; Maiheu, B.; van Heijst, G. A review on the CFD analysis of urban microclimate. *Renew. Sustain. Energy Rev.* **2017**, *80*, 1613–1640. [[CrossRef](#)]
40. Launder, B.E.; Spalding, D.B. The numerical computation of turbulent flows. *Comput. Methods Appl. Mech. Eng.* **1974**, *3*, 269–289. [[CrossRef](#)]
41. Yamada, T.; Mellor, G. A Simulation of the Wangara Atmospheric Boundary Layer Data. *J. Atmos. Sci.* **1975**, *32*, 2309–2329. [[CrossRef](#)]
42. Revuz, J.; Hargreaves, D.; Owen, J. On the domain size for the steady-state CFD modelling of a tall building. *Wind. Struct.* **2012**, *15*, 313–329. [[CrossRef](#)]
43. Franke, J.; Hirsch, C.; Jensen, A.; Krüs, H.; Schatzmann, M.; Westbury, P.; Wright, N. Recommendations on the use of CFD in wind engineering. In *Impact of Wind and Storm on City Life Built Environment. Proceedings of the International Conference on Urban Wind Engineering and Building Aerodynamics*; COST Action C14; van Beeck, J.P.A.J., Ed.; Von Karman Institute: Sint-Genesius-Rode, Belgium, 2004.

Disclaimer/Publisher’s Note: The statements, opinions and data contained in all publications are solely those of the individual author(s) and contributor(s) and not of MDPI and/or the editor(s). MDPI and/or the editor(s) disclaim responsibility for any injury to people or property resulting from any ideas, methods, instructions or products referred to in the content.